Spectral Domain Green's Function of an Infinite Dipole With Nonzero Metal Thickness and Rectangular Cross Section

Speksnijder, Erik; Ozzola, Riccardo; Neto, Andrea

DOI
10.1109/TMTT.2024.3361532

Publication date
2024

Document Version
Final published version

Published in
IEEE Transactions on Microwave Theory and Techniques

Spectral Domain Green's Function of an Infinite Dipole With Nonzero Metal Thickness and Rectangular Cross Section

Erik A. Speksnijder, Riccardo Ozzola, *Graduate Student Member, IEEE*, and Andrea Neto, *Fellow, IEEE*

***Abstract*— The calculation of the transmission line Green's function (TL GF) of an infinite metal line of rectangular cross section embedded in a generalized stratification is presented. The proposed procedure is quasi-analytical and extends prior models to account effectively for the nonzero thickness of the conductors. From Green's function of an infinite dipole, an equivalent network is derived to represent the current propagating along the dipole and the reactive loading due to the feeding gap dimensions. The method is validated with numerical simulations and available experimental results. Examples of dipoles in free space, microstrips, and leaky dipoles are shown.**

***Index Terms*— Dipole, equivalent circuit, Green's function, microstrip, skin effect, spectral domain representation.**

I. Introduction

THE analysis of printed dipoles and microstrips has been the subject of a large body of the scientific literature [1]. Nowadays, there are several commercial tools [2], [3], [4], [5] that can easily provide an accurate estimation of the characterizing parameters. Moreover, to increase the speed and accuracy of the analysis, in the last 30 years, transmission line Green's functions (TL GF) have emerged [6], [7], [8], [9], [10], [11]. These can perform an efficient analysis and provide physical insight into the dispersion properties of open-ended lines. In fact, relying on these transmission line GF, antennas, such as leaky wave lenses [12], slots [13], and connected arrays [14], are nowadays routinely designed.

The Terahertz Sensing Group has developed a user-friendly code [15] that implements the TL GF for the most used open line configurations, as described in [16]. These latter lines have become relevant with the advances of sub-millimeter wave architectures and the corresponding micrometric sizes. Unfortunately, the TL GF formulation cannot include the metal thickness as a characterizing parameter to date. The metal thickness can be a design parameter if one wishes, for instance, to realize a resistor or, on the contrary, minimize the losses in an integrated transmission line. In this article, a TL GF formulation for dipoles of nonzero metal thickness embedded in general stratifications is described. Our formulation models the current in the cross section with a single basis function, as [6], [8], and [16]; however, the basis function also represents the vertical current profile.

The spectral domain formulation, similar to [6] and [8], allows to derive the current spectrum, and from this, the characteristic impedance, the propagation constant, and the losses of the line are extracted. In addition, a transmission line equivalent circuit is introduced to characterize the input impedance of the dipole. The circuit includes a term associated with the characteristic impedance of the line and the reactance associated with the delta-gap excitation, which is dependent on the cross section and the length of the gap.

This article is structured as follows. In Section II, the formulation is presented in Section III, the results regarding the propagation in a dipole in free space, in a microstrip, and in a printed dipole are discussed, and finally, in Section IV, the transmission line equivalent circuit is derived, and an example is presented. Part of the mathematical derivation is discussed in the appendixes to ease the readability.

II. Formulation

The formulation in this section extends [6], [8], and [16] to account for the thickness of the metal. All the steps are included to highlight the assumptions and the approximations used in this article.

Let us consider the infinitely long dipole shown in Fig. 1(a) and (b), embedded in an arbitrary stratification, oriented along the x-axis, constituted by a homogeneous material having a conductivity σ (or equivalently a resistivity $\rho = 1/\sigma$), having a rectangular cross section A, w_y wide, and w_z thick, and excited by a feeding port Δ long. If the port is sufficiently small, the fringing of the incident field can be neglected, and it can be considered as a Δ-gap generator, where the field is assumed to be uniform. The current flowing in the dipole is assumed to have only the axial component, i.e., oriented along $\hat{x}$. As the width of the dipole is much smaller than the wavelength, the separation of variables can be applied

Manuscript received 18 January 2024; accepted 24 January 2024. Date of publication 13 February 2024; date of current version 7 August 2024. *(Corresponding author: Riccardo Ozzola.)*

Erik A. Speksnijder was with the Microelectronics Department, Electrical Engineering, Mathematics and Computer Science Faculty, Delft University of Technology, 2628 CD Delft, The Netherlands. He is now with TNO Defence Security and Safety, 2597 AK The Hague, The Netherlands.

Riccardo Ozzola and Andrea Neto are with the Microelectronics Department, Electrical Engineering, Mathematics and Computer Science Faculty, Delft University of Technology, 2628 CD Delft, The Netherlands (e-mail: R.Ozzola-1@tudelft.nl).

This article has supplementary material provided by the authors and color versions of one or more figures available at https://doi.org/10.1109/TMTT.2024.3361532.

Digital Object Identifier 10.1109/TMTT.2024.3361532

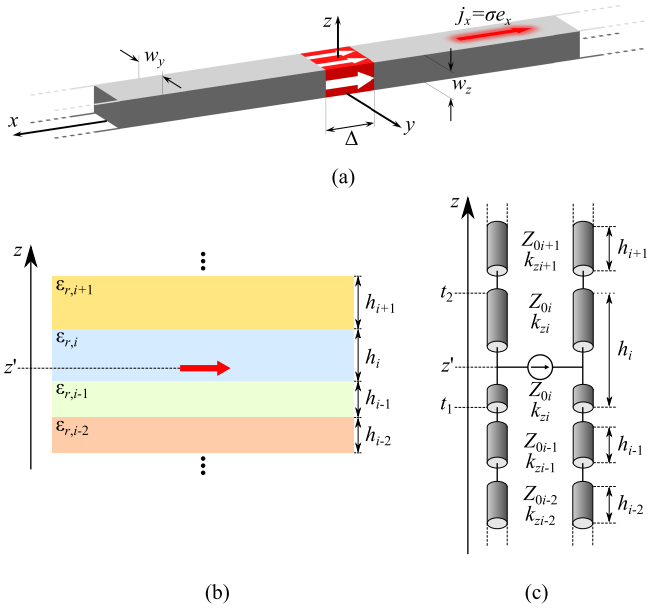

Fig. 1. (a) Sketch of an infinitely long dipole oriented along x, w_y wide, and w_z thick, and excited by a δ-gap generator Δ long, (b) vertical section of the dipole in an arbitrary stratification, and (c) transmission line equivalent representation of the stackup.

in the cross section. By resorting to the local form of Ohm's law, i.e., $\vec{j} = \sigma\vec{e}$, by expressing the total field as the sum of the incident and the scattered one, the following expression is obtained:

$$\rho\, i(x) j_t(y,z) = v(x) e_t^i(y,z) + e_x^s(x,y,z) \tag{1}$$

where $i(x)$ and $j_t(y,z)$ are the longitudinal and transverse dependencies of the current distribution, respectively, $v(x)$ and $e_t^i(y,z)$ are the longitudinal and transverse expressions of the incident field, and $e_x^s(x,y,z)$ is the x-component of the scattered field. As the excitation is modeled as a Δ-gap generator Δ long, $v(x)$ and $e_t^i(y,z)$ can be written as follows:

$$v(x) = \frac{V_0}{\Delta}\,\mathrm{rect}\left(\frac{x}{\Delta}\right) \tag{2}$$

$$e_t^i(y,z) = \mathrm{rect}\left(\frac{y}{w_y}\right)\mathrm{rect}\left(\frac{z}{w_z}\right) \tag{3}$$

where rect is the rectangular pulse, i.e., $\mathrm{rect}(x) := 1$ $\forall |x| < 1/2$, and V_0/Δ is the magnitude of the incident field on the gap. By isolating the incident field on the left-hand side and by expressing the scattered field as the radiation from the currents on the dipole, one can write the following expression:

$$\frac{V_0}{\Delta}\,\mathrm{rect}\left(\frac{x}{\Delta}\right) e_t^i(y,z) = \rho\, i(x) j_t(y,z) - g_{xx}^{EJ}(x,y,z) * \left[i(x) j_t(y,z)\right] \tag{4}$$

where $g_{xx}^{EJ}(x,y,z)$ is the stratified media space Green's function providing the electric field from the electric currents, and the symbol $*$ is a spatial convolution which in its extended form has the following expression:

$$\int_{-\infty}^{+\infty}\int_{-w_y/2}^{w_y/2}\int_0^{w_z}\left[g_{xx}^{EJ}(x-x', y-y', z-z') \times i(x') j_t(y',z')\right]dx'dy'dz'. \tag{5}$$

Green's function g_{xx}^{EJ} in (5) can be expressed in the spectral domain as follows:

$$g_{xx}^{EJ}(x-x', y-y', z-z') = \frac{1}{4\pi^2}\int_{-\infty}^{+\infty}\int_{-\infty}^{+\infty}\left[G_{xx}^{EJ}(k_x,k_y,z,z') \times e^{-jk_x(x-x')} e^{-jk_y(y-y')}\right]dk_x dk_y \tag{6}$$

where $G_{xx}^{EJ}(k_x,k_y,z,z')$ is the spectral domain stratified media Green's function, with k_x and k_y being the wavenumber domain counterparts of the x- and y-coordinates, and which is known [17, Appendix A.3] having the following analytical expression:

$$G_{xx}^{EJ}(k_x,k_y,z,z') = -\frac{v_{\mathrm{TM}}(z,z')k_x^2 + v_{\mathrm{TE}}(z,z')k_y^2}{k_x^2+k_y^2} \tag{7}$$

where $v_{\mathrm{TM}}(z,z')$ and $v_{\mathrm{TE}}(z,z')$ are the voltage solutions at z of the TM and TE transmission line equivalent problems, as shown in Fig. 1(c), when the sources are placed at z'. Their calculation is carried out as in [17, Appendix A].

Thanks to the rectangular cross section, the separation of variables can be applied, and the dependence of the transverse current distribution j_t can be written as follows:

$$j_t(y,z) = j_{t,y}(y) j_{t,z}(z). \tag{8}$$

By substituting (6) into (5), one can calculate the Fourier transforms of i and j_t with respect to x' and y', and obtaining the following expression for the scattered field:

$$e_x^s(x,y,z) = \frac{1}{4\pi^2}\int_{-\infty}^{+\infty}\int_{-\infty}^{+\infty}\int_0^{w_z}\left[G_{xx}^{EJ}(k_x,k_y,z,z') \times I(k_x) J_{t,y}(k_y) j_{t,z}(z') e^{-jk_x x} e^{-jk_y y}\right]dk_x dk_y dz' \tag{9}$$

where $I(k_x)$ is the Fourier transform of i, performed with respect to x, and $J_{t,y}(k_y)$ is the Fourier transform of $j_{t,y}(y)$. One can more conveniently express (4) in the spectral domain, where the spectra in k_x can be equated as for infinitely long dipoles, the equality holds for every x, yielding

$$V_0\,\mathrm{sinc}\left(\frac{k_x\Delta}{2}\right) e_t^i(y,z) = I(k_x)\left[\rho j_t(y,z) - \frac{1}{2\pi}\int_{-\infty}^{+\infty}\int_0^{w_z} G_{xx}^{EJ}(k_x,k_y,z,z') \times J_{t,y}(k_y) j_{t,z}(z') e^{-jk_y y} dk_y dz'\right]. \tag{10}$$

One can first define the following projection operator:

$$\langle f, g\rangle_A = \iint_A f(y,z) g^*(y,z) dy dz \tag{11}$$

and can then project the left and the right-hand side of (10) on the test function $\tilde{j}_t$, which is expressed as follows:

$$\tilde{j}_t(y,z) = \tilde{j}_{t,y}(y)\tilde{j}_{t,z}(z). \tag{12}$$

This can be defined by having a unitary flux on the cross section, i.e., $\langle \tilde{j}_t, e_t^i\rangle_A = 1$, and therefore, the Fourier transform of the current I along the dipole can be calculated as follows:

$$I(k_x) = \frac{V_0\,\mathrm{sinc}(k_x\Delta/2)}{D(k_x)} \tag{13}$$

where sinc $:= \sin(x)/x$ is the Fourier transform of the rect function, and D is the transverse Green's function of the dipole, defined in the following manner:

$$D(k_x) = \rho\langle j_t, \tilde{j}_t\rangle_A - \frac{1}{2\pi}\int_{-\infty}^{+\infty}\int_0^{w_z}\int_0^{w_z} \left[G_{xx}^{EJ}(k_x, k_y, z, z') \times J_{t,y}(k_y)\tilde{J}_{t,y}(-k_y) j_{t,z}(z')\tilde{j}_{t,z}^*(z)\right] \times dz dz' dk_y. \tag{14}$$

By taking advantage of the formulation in [18, eq. (72)], whose steps are reported for the sake of completeness in Appendix A, the integrals in z and z' can be closed analytically for suitable choices of j_t and $\tilde{j}_t$. For the specific choice of the basis functions used in this article, their analytical result of (14) is reported in the supplementary material. The current distribution along y in (8) can be defined by having the following edge singular behavior as in [8]:

$$j_{t,y}(y) = \frac{2}{\pi w_y}\frac{1}{\sqrt{1-\left(\frac{2y}{w_y}\right)^2}}\,\mathrm{rect}\left(\frac{y}{w_y}\right). \tag{15}$$

and for (12) as follows:

$$\tilde{j}_{t,y}(y) = \frac{\mathrm{rect}(y/w_y)}{w_y} \tag{16}$$

to allow for the convergence when calculating the projections in (14).

A. Profile of the Currents Along z

The choice of $j_{t,z}$ in (8) and $\tilde{j}_{t,z}$ in (12) must take into account the stratification where the dipole is embedded in, as imbalanced currents flow on the top and bottom parts of the metal. To this aim, the current flow is split into two distributions, each representing a wave propagating in a lossy metal [19]. The current distributions on the bottom and top parts of the metal, respectively, are as follows:

$$j_{t,1}(y,z) = \frac{(1+j)j_{t,y}(y)e^{-(1+j)z/\delta_p}}{\delta_p\left(1-e^{-(1+j)w_z/\delta_p}\right)} \times \mathrm{rect}\left(\frac{z-w_z/4}{w_z/2}\right) \tag{17}$$

$$j_{t,2}(y,z) = \frac{(1+j)j_{t,y}(y)e^{-(1+j)(z-w_z)/\delta_p}}{\delta_p\left(1-e^{(1+j)w_z/\delta_p}\right)} \times \mathrm{rect}\left(\frac{z-3w_z/4}{w_z/2}\right) \tag{18}$$

where δ_p is the penetration depth, and as sketched in Fig. 2. When the penetration depth becomes comparable with w_z, the current profile along z has to include also the multiple reflections at the interfaces, which are not accounted for in the proposed method. In fact, to obtain a semianalytical solution, the current is approximated with a reduced number of basis functions. In addition to this, to ease the analytical calculations, due to its compact Fourier transform, we have chosen for the current distribution along y the edge singular distribution (15), which does not depend on δ_p. Therefore, these assumptions imply approximated results in the low-frequency regime. By performing the projections on the test

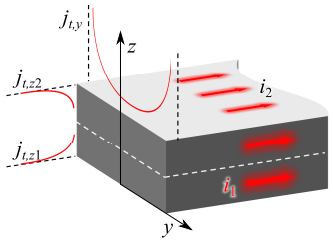

Fig. 2. Sketch of the current distribution on the dipole, highlighting the y-dependent distribution $j_{t,y}(y)$, the z-dependent distributions $j_{t,z1}(z)$ and $j_{t,z2}(z)$, and the currents on the axis $i_1(x)$ and $i_2(x)$.

functions $\tilde{j}_{t,1}$ and $\tilde{j}_{t,2}$, which are the split-current counterpart of (12), the following matrix equation is written:

$$\begin{bmatrix}V_1(k_x)\\ V_2(k_x)\end{bmatrix} = \begin{bmatrix}\langle e_t^i, j_{t,1}\rangle_A\\ \langle e_t^i, j_{t,2}\rangle_A\end{bmatrix}\mathrm{sinc}\left(\frac{k_x\Delta}{2}\right) = \begin{bmatrix}D_{11}(k_x) & D_{12}(k_x)\\ D_{21}(k_x) & D_{22}(k_x)\end{bmatrix}\begin{bmatrix}I_1(k_x)\\ I_2(k_x)\end{bmatrix} \tag{19}$$

with $I_1(k_x)$ and $I_2(k_x)$ being the spectrum of the currents flowing on the bottom and top sides, respectively, as shown in Fig. 2. The entries $D_{mn}(k_x)$ are defined in the following manner:

$$D_{mn}(k_x) = \rho\langle j_{t,m}, \tilde{j}_{t,n}\rangle_A - \frac{1}{2\pi}\int_{-\infty}^{+\infty}\int_0^{w_z}\int_0^{w_z} \left[G_{xx}^{EJ}(k_x, k_y, z, z') \times J_{t,y}(k_y)\tilde{J}_{t,y}(-k_y) j_{t,zm}(z')j_{t,zn}^*(z)\right] dz dz' dk_y \tag{20}$$

and by resorting to [18] to express the stratified media Green's function, thanks to the chosen current distributions, the space-domain integrals of (20) can be solved analytically. The solution of (19) is given in the following expressions:

$$I_1(k_x) = \frac{D_{22}(k_x)V_1(k_x) - D_{12}(k_x)V_2(k_x)}{\det(\mathbf{D}(k_x))} \tag{21}$$

$$I_2(k_x) = \frac{D_{11}(k_x)V_1(k_x) - D_{21}(k_x)V_2(k_x)}{\det(\mathbf{D}(k_x))} \tag{22}$$

where $\det(\mathbf{D}(k_x))$ is the 2×2 matrix determinant. By solving the dispersion equation $\det(\mathbf{D}(k_x)) = 0$, one can find the two poles $k_{xp,1}$ and $k_{xp,2}$. This allows us to interpret the currents propagating on either the top or bottom part as the superposition of two contributions expressed as follows:

$$i_{1,\mathrm{res},h}(x) = -j\frac{D_{22}V_1 - D_{12}V_2}{(\det(\mathbf{D}))'}e^{-jk_x x}\Big|_{k_x=k_{xp,h}} \tag{23}$$

$$i_{2,\mathrm{res},h}(x) = -j\frac{D_{11}V_1 - D_{21}V_2}{(\det(\mathbf{D}))'}e^{-jk_x x}\Big|_{k_x=k_{xp,h}} \tag{24}$$

where the index h denotes either pole 1 or pole 2. The current on either the bottom (23) or the top (24) of the dipole is the superposition of the modes associated with pole 1 and pole 2. By calculating the imbalance between the currents as follows:

$$R = \frac{i_{1,\mathrm{res},1}(x) + i_{1,\mathrm{res},2}(x)}{i_{2,\mathrm{res},1}(x) + i_{2,\mathrm{res},2}(x)}\Big|_{x=0} \tag{25}$$

one can write a single asymmetric transverse current distribution as follows:

$$j_{t,z}(z) = \frac{(1+j)\left(R\,e^{-(1+j)z/\delta_p} + e^{(1+j)(z-w_z)/\delta_p}\right)}{\delta_p(R+1)e^{-(1+j)w_z/\delta_p}\left(e^{(1+j)w_z/\delta_p}-1\right)} \times \text{rect}\left(\frac{z-w_z/2}{w_z}\right) \tag{26}$$

to be used in (8) to calculate the transverse Green's function (14), to be used in the current spectrum (13). The analytical solution of the integrals of (14) involving (26), is given in the supplementary material.

III. Results

This section discusses the applications of the formulation derived in Section II.

A. Dipole in Free Space

For a dipole in free space, due to the symmetry of the problem, the parameter R from (25) is equal to unity, resulting in the following current profile along z:

$$j_{t,z}(z) = \frac{(1+j)\left(e^{-(1+j)z/\delta_p} + e^{(1+j)(z-w_z)/\delta_p}\right)}{2\delta_p e^{-(1+j)w_z/\delta_p}\left(e^{(1+j)w_z/\delta_p}-1\right)} \times \text{rect}\left(\frac{z-w_z/2}{w_z}\right) \tag{27}$$

and where the following free-space Green's function is used:

$$G_{xx}^{EJ} = -\frac{j\zeta}{k}\frac{k^2-k_x^2}{\sqrt{k^2-k_x^2-k_y^2}}. \tag{28}$$

The current distribution $i(x)$ can be found by calculating the following inverse Fourier transform:

$$i(x) = \frac{1}{2\pi}\int_{-\infty}^{+\infty}\frac{V_0\,\text{sinc}(k_x\Delta/2)}{D(k_x)}e^{-jk_x x}dk_x \tag{29}$$

where the integration path C_R has been deformed around the real axis to avoid the square-root branch cuts in the k_x-plane, as shown in Fig. 3(a). The region of convergence (RoC) of (29) depends on the observation point x. If $x < 0$ the convergence is guaranteed for $\text{Im}\{k_x\} > 0$, otherwise for $x > 0$ in the half-plane $\text{Im}\{k_x\} < 0$, therefore, the path needed to close the integral at infinity has to be chosen accordingly, as shown in Fig. 3(a), and depending on the path either the pole k_{xp} or $-k_{xp}$ results enclosed.

As an example, the current is calculated at $f = 300$ GHz for a dipole excited with 1 V and having $w_y = w_z = 10\,\mu$m, $\Delta = 20\,\mu$m, and $\sigma = 10^6$ S/m, resulting in a good agreement with CST, as reported in Fig. 3(b). As shown, the residue contribution alone does not fully represent the current along the dipole at a large distance from the feed. As shown in [20] and [21], an infinite dipole in free space also supports a space wave with logarithmic decay.

B. Microstrip

Unlike the dipoles in homogeneous space, some topologies support a dominant residue contribution. For instance, if the dipole is backed by a ground plane, the radiation from the feed is negligible, and thus, the residue contribution provides the dominant propagating wave. The effective permittivity and the losses associated with the propagating mode are shown in Fig. 4 for different metal widths and thicknesses.

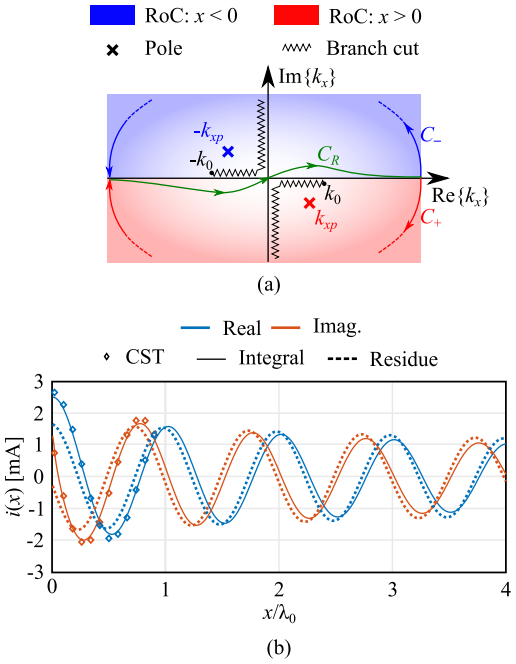

Fig. 3. (a) Complex plane topology for (29) and (b) current along a dipole in free space calculated with the inverse Fourier transform of (13), with the residue contribution, and CST for $w_y = w_z = 10\,\mu$m, $\Delta = 20\,\mu$m, and $\sigma = 1 \times 10^6$ S/m, and having unitary excitation.

For the topologies that support a dominant residue contribution, i.e., dipoles embedded in stratifications that significantly alter the propagation constant with respect to free space, a characteristic impedance Z_0 can be defined for the mode associated with the residue, defined as in [22] and [23] as follows:

$$Z_0 = j\frac{D'(k_{xp})}{2}. \tag{30}$$

The characteristic impedance is instrumental for the definition of an equivalent circuit that can be used to accurately characterize the impact of the dimensions of the feeding gap.

The characteristic impedance Z_0 is evaluated for the dipole as shown in Fig. 5. It is constituted by a material of conductivity $\sigma = 4.11 \times 10^7$ S/m, and it is printed over a grounded slab thick $d = 10\,\mu$m having a relative permittivity $\varepsilon_r = 4.3$. Given the topology, it is a microstrip. Fig. 5(a) and (b) shows the impact of the metal thickness w_z on the real part of the characteristic impedance for different values of the width w_y. As expected, the values of Z_0 increase by reducing the width w_y and the metal thickness w_z. The impact of w_z on the characteristic impedance is larger when it starts to be comparable with w_y, producing a variation of 12% for $w_y = 5\,\mu$m for the minimum considered thickness. The results produced with the method presented here are compared with the ones obtained with [15], which does not consider the thickness w_z. The results are also compared with the ones obtained using the commercial tool Sonnet [2]. In both cases, there is a fair agreement. The attenuation constant is shown

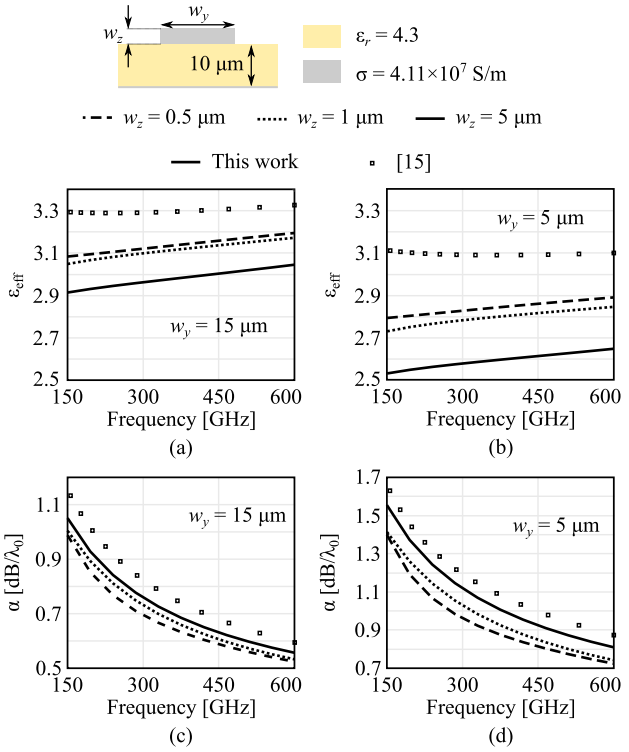

Fig. 4. Effective permittivity for (a) $w_y = 15$ μm and (b) $w_y = 5$ μm and attenuation constant for (c) $w_y = 15$ μm and (d) $w_y = 5$ μm of a dipole constituted by a material of conductivity $\sigma = 4.11 \times 10^7$ S/m, printed over a grounded slab thick $d = 10$ μm for different values of the metal thickness w_z.

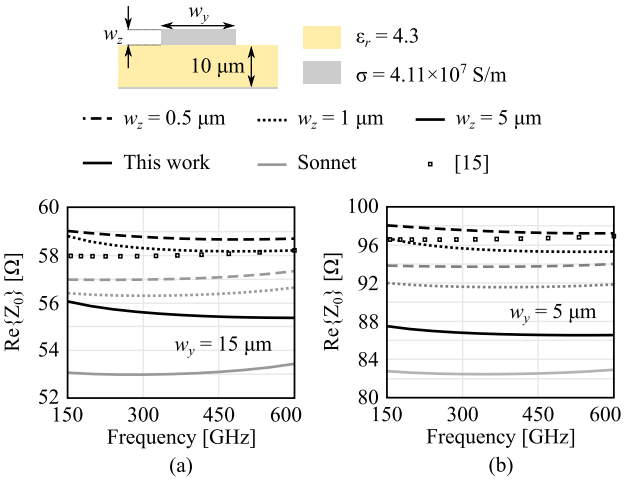

Fig. 5. Real part of the characteristic impedance for (a) $w_y = 15$ μm and (b) $w_y = 5$ μm and attenuation constant for (c) $w_y = 15$ μm and (d) $w_y = 5$ μm of a dipole constituted by a material of conductivity $\sigma = 4.11 \times 10^7$ S/m, printed over a grounded slab thick $d = 10$ μm for different values of the metal thickness w_z.

in Fig. 5(c) and (d) for $w_y = 15$ μm and $w_y = 5$ μm, respectively. The losses slightly increase by decreasing w_y, and their dependence on the thickness is minor.

As a further validation of the accuracy of the presented method, we compare in Fig. 6 our method with the measurements and the simulations of [24], which presents the state-of-the-art numerical tool [2] for modeling microstrip lines and their losses. The line has a length of 6.888 mm,

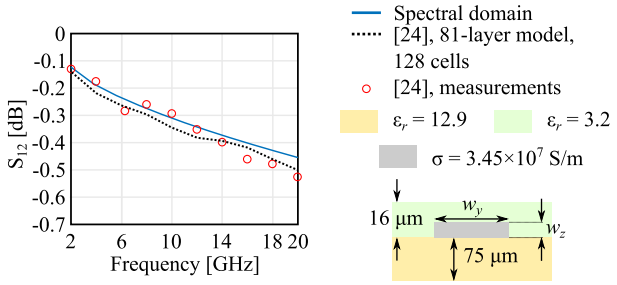

Fig. 6. S_{12} comparison between the measurements and the simulations of the 81-layer model with 128 cells of [24] and the spectral domain characterization.

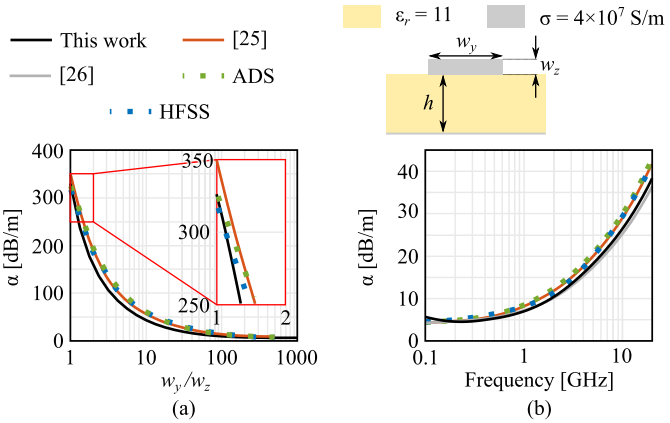

Fig. 7. (a) Conductor losses versus the aspect ratio of the metal at 9 GHz, for a microstrip of thickness $w_z = 1.524$ μm and conductivity $\sigma = 4 \times 10^7$ S/m, when printed on a dielectric having a permittivity $\varepsilon_r = 11$ and thickness $h = 254$ μm. (b) Conductor losses versus the frequency for a microstrip of thickness $w_z = 6$ μm, width $w_y = 152.4$ μm, and a conductivity $\sigma = 4 \times 10^7$ S/m, when printed on a substrate of thickness $h = w_y/2$ and permittivity $\varepsilon_r = 11$.

a width $w_y = 51$ μm and a thickness $w_z = 7$ μm, it is constituted by a material of $\sigma = 3.45 \times 10^7$ S/m printed at the interface between two dielectrics having permittivity 12.9 and 3.2, and thickness 75 and 16 μm, respectively. The comparison shows an excellent agreement between the measurements and the two simulations. However, the minor differences between the spectral domain method and the numerical solution of [24] could be attributed to how the currents are modeled over the cross section. In fact, in [24], the current in the microstrip is divided into 81 layers along z and 128 cells along y, while for the method here proposed, we resort to (15) and (26), which allows us to derive a semianalytical solution.

Our method is also tested with the conductor losses of [25], [26] obtained with the concept of the quasi-transverse electromagnetic surface impedance. In Fig. 7(a), we reproduce [25, Fig. 7], which shows the attenuation constant of a microstrip at 9 GHz versus the aspect ratio w_y/w_z for a thickness $w_z = 1.524$ μm and conductivity $\sigma = 4 \times 10^7$ S/m, when printed on a dielectric having a permittivity $\varepsilon_r = 11$ and thickness $h = 254$ μm. The results of [25] are in better agreement with the ones obtained with the commercial tools HFSS and ADS. However, the present tool allows for a better agreement with both the reference tools for small aspect ratios, i.e., $w_y/w_z \approx 1$, which is the condition where [25] commits the largest error. In Fig. 7(b), we reproduce [25, Fig. 6] by showing

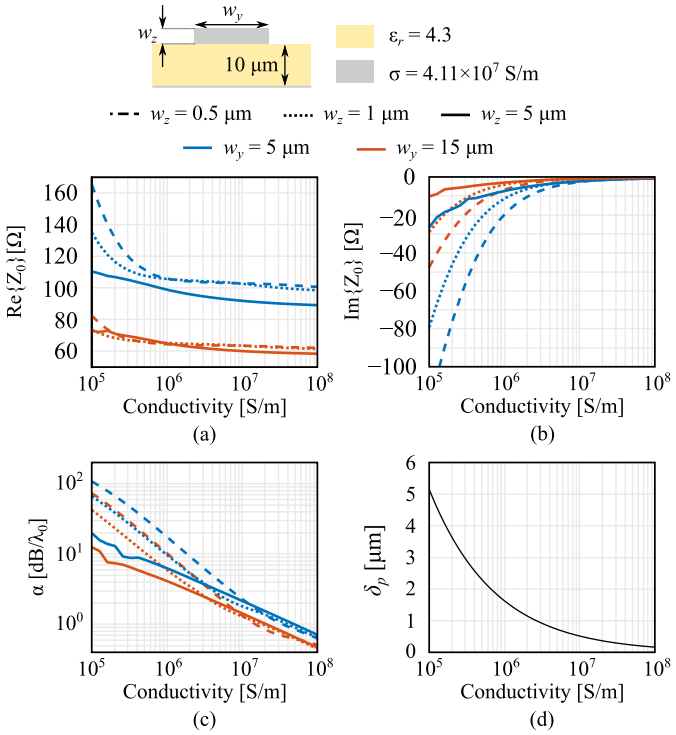

Fig. 8. (a) Real and (b) imaginary parts of the characteristic impedance, and (c) attenuation constant versus the metal conductivity calculated at 300 GHz, for a microstrip of width w_y and w_z thick printed on a dielectric $h = 10$ μm-thick and having dielectric permittivity $\varepsilon_r = 4.3$. (d) Penetration depth versus the conductivity calculated at 300 GHz.

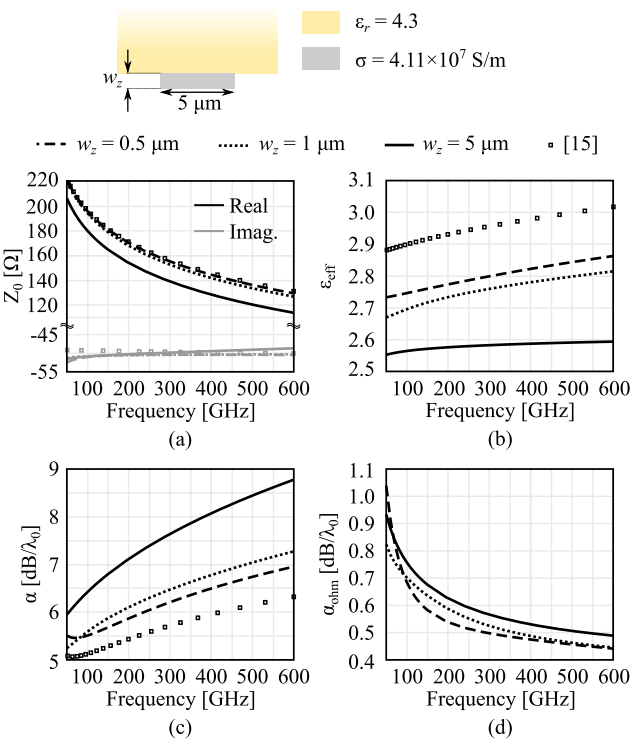

Fig. 9. (a) Characteristic impedance, (b) effective permittivity, (c) total attenuation constant, and (d) attenuation constant of the ohmic losses associated with a leaky mode supported on a dipole constituted by a metal of conductivity $\sigma = 4.11 \times 10^7$ S/m, width $w_y = 5$ μm, and thickness w_z, and printed on a semi-infinite dielectric medium of permittivity $\varepsilon_r = 4.3$.

the attenuation constant versus the frequency for a microstrip of thickness $w_z = 6$ μm, width $w_y = 152.4$ μm, and a conductivity $\sigma = 4 \times 10^7$ S/m, when printed on a substrate of thickness $h = w_y/2$ and permittivity $\varepsilon_r = 11$. The results obtained by Hamham et al. [25] are in better agreement with the reference tools than the spectral domain, which is superimposed with [26].

The impact of the conductivity σ on the characteristic impedance is investigated in Fig. 8, where the characteristic impedance Z_0 and the attenuation constant α are studied at 300 GHz for different widths and thicknesses of the microstrip when it is printed on a dielectric of permittivity $\varepsilon_r = 4.3$ and thickness $h = 10$ μm. As shown in Fig. 8(a), the real part of the characteristic impedance depends mainly on the width of the line w_y, and, for smaller values of σ, also this latter and w_z starts to have an impact. The imaginary part of Z_0 is shown in Fig. 8(b), exhibiting large negative values, i.e., high losses for smaller values of σ. The attenuation constant α is shown in Fig. 8(c). In good conductors α is mainly due to σ and w_y, and weakly dependent on w_z. Instead, for low values of σ, also the metal thickness plays an important role in the attenuation constant. It is worth mentioning that, as previously stated the results are affected by the penetration depth [see Fig. 8(d)] becoming comparable with the other dimensions in the geometry.

C. Printed Leaky Dipoles

As a final example, we consider the case of a dipole printed between free space and a dielectric half-space. In this case, the propagation is much more dispersive with respect to frequency due to the excitation of a dominant leaky wave. The dispersion can be appreciated by looking at the characteristic impedance in Fig. 9(a), where the significant imaginary part indicates the radiation losses. The real part of the effective propagation constant is shown in Fig. 9(b), where it is noticeable that the predictions of the present tool associate a significant impact on the thickness of the metal, which is disregarded in the tool in [15] and [16]. Finally, the attenuation versus the frequency is shown in Fig. 9(c) and (d). The radiation-induced losses are clearly the main cause of the attenuation, as shown in Fig. 9(d).

As it can be seen from Fig. 9(b), the effective permittivity decreases when increasing the metal thickness, as a larger share of the current is located in free space. However, the effective permittivity depends on the average between the permittivities of the dielectrics above and below the dipole. Therefore, the propagation along a thick metal dipole can be equivalently reproduced on a planar line located between one of the two original dielectrics and a less dense one. As an example, in Fig. 10, the permittivity of the dipoles of Fig. 9 are synthesized using [15] by decreasing the permittivity of the dielectric from $\varepsilon_r = 4.3$ to $\varepsilon_r = 4.05$ and $\varepsilon_r = 3.97$, and $\varepsilon_r = 3.65$ to obtain the same effective permittivity of $w_z = 0.5$ μm, $w_z = 1$ μm, and $w_z = 5$ μm, respectively. The bandwidth in which the synthesis is valid decreases with the metal thickness.

IV. Transmission Line Equivalent Circuit

Once the TL GF is validated, it is useful to look at the dominant spectral components of the current, highlighting the

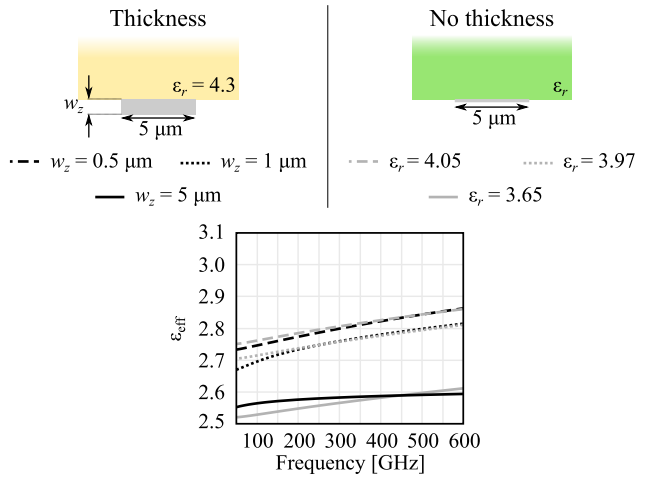

Fig. 10. Synthesis of the effective permittivity in dipoles with nonzero metal thickness by using planar dipoles printed on a different medium.

impact of the low and high parts of the spectrum. These are then used to derive an equivalent circuit that represents the input impedance of a Δ-gap fed dipole.

A. Spectral Components of the Current

In the case of a dominant polar contribution, the current spectrum (13) can be approximated around the pole k_{xp} with its Laurent expansion. This constitutes the dynamic component of the current I_{dyn}, which is expressed as follows:

$$I(k_x) \approx I_{\text{dyn}}(k_x) = \frac{2k_{xp}\,\text{sinc}(k_x\Delta/2)}{D'(k_{xp})(k_x^2 - k_{xp}^2)} \quad \text{for } k_x \to k_{xp}. \tag{31}$$

By performing analytically the inverse Fourier transform of (31), as in Appendix B, the dynamic current component can be written, outside the feeding gap, as the following traveling wave:

$$i_{\text{dyn}}(|x| > \Delta/2) = -j\frac{\text{sinc}(k_{xp}\Delta/2)}{D'(k_{xp})}e^{-jk_{xp}|x|} \tag{32}$$

and inside the gap as the following standing wave:

$$i_{\text{dyn}}(|x| < \Delta/2) = 2\frac{1-\cos(k_{xp}x)e^{-jk_{xp}\Delta/2}}{\Delta k_{xp}D'(k_{xp})}. \tag{33}$$

In Fig. 11, the dynamic current is compared with the total current at $f = 300$ GHz in a dipole constituted by a metal with conductivity $\sigma = 4.11 \times 10^7$ S/m of width $w_y = 30$ μm, and printed on a grounded dielectric slab with permittivity $\varepsilon_r = 4.3$ and thickness $d = 10$ μm for two values of the gap-size Δ and the metal thickness w_z. Inside and outside the gap area, the dynamic current is associated with variations dominated by the wavenumber k_{xp}. If away from the gap, the total and the dynamic currents are superimposed, close to the gap, the imaginary part of the current is significantly different from the dynamic one, especially for smaller gap sizes. This has to be imputed to the current's high-spectrum component, which is not taken into account in (31) and becomes more important when decreasing the gap size.

The quasi-static component of I, i.e., for $k_x \to \infty$, can be approximated by an asymptotic expression for D, as shown in

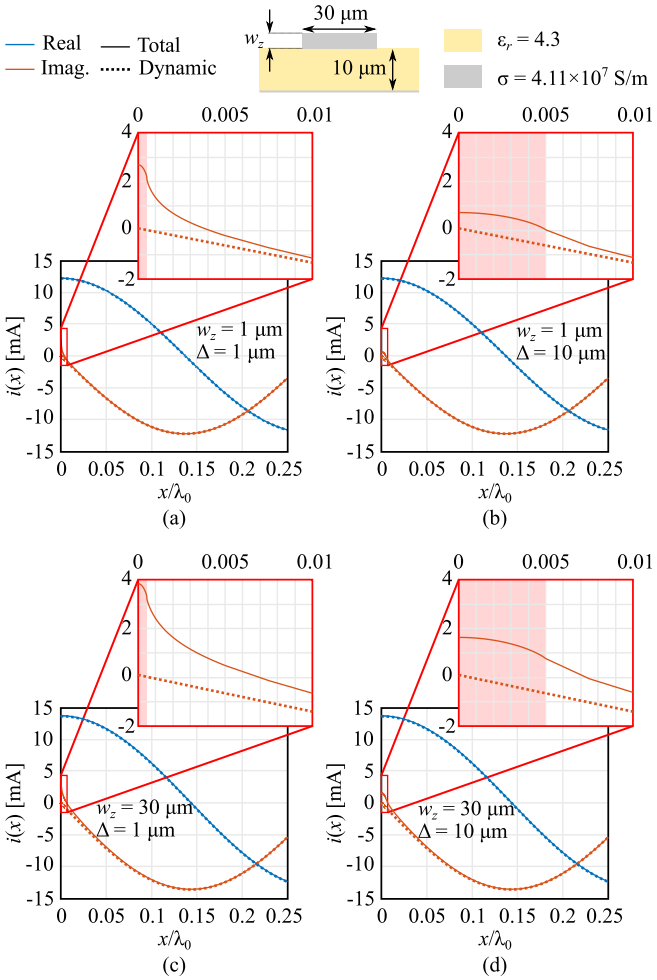

Fig. 11. Comparison between the total and the dynamic currents at $f = 300$ GHz in a dipole constituted by a metal with conductivity $\sigma = 4.11 \times 10^7$ S/m and width $w_y = 30$ μm, and printed on a grounded dielectric slab with permittivity $\varepsilon_r = 4.3$ and thickness $d = 10$ μm for (a) $\Delta = 1$ μm and $w_z = 1$ μm, (b) $\Delta = 10$ μm and $w_z = 1$ μm, (c) $\Delta = 1$ μm and $w_z = 30$ μm, and (d) $\Delta = 10$ μm and $w_z = 30$ μm. The gap is highlighted in the red-shaded areas in the insets.

Appendix C, which yields to the following expression:

$$D(k_x) \approx D_\infty(k_x) = \rho\langle j_t, \tilde{j}_t\rangle_A - \frac{J_{t,y}(0)}{w_y}\int_0^{w_z}\int_0^{w_z}\left[G_{xx}^{EJ}(k_x,0,z,z')j_{t,z}(z')j_{t,z}(z)\right] \times dzdz' \quad \text{for } k_x \to \infty. \tag{34}$$

In Fig. 12, the relative error between D and D_∞, i.e., $|D - D_\infty|/|D|$ is shown versus k_x for different values of the width w_y. The convergence rate increases with w_y, as for smaller values, the decay in (69) is slower.

B. Dynamic Admittance

Once the nature of the current is established, it suggests deriving the equivalent circuit for the input impedance of a delta gap fed dipole. The ideas are similar to those discussed in [13], [27], [28], and [29]. With respect to those cases, the presentation here allows us to highlight the impact of the metal

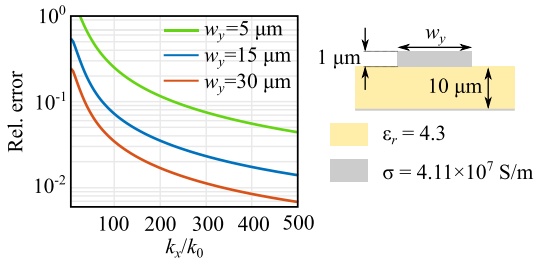

Fig. 12. Relative error between D and D_∞ versus k_x calculated for different values of w_y for a dipole constituted by a metal with conductivity $\sigma = 4.11 \times 10^7$ S/m of thickness $w_z = 1$ μm, and printed on a grounded dielectric slab with permittivity $\varepsilon_r = 4.3$ and thickness $d = 10$ μm.

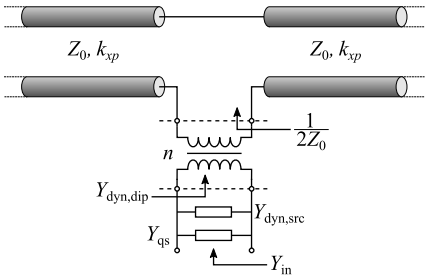

Fig. 13. Transmission line equivalent circuit of an infinitely long dipole, represented by two transmission line sections placed in series and connected to a transformer, constituting $Y_{dyn,dip}$, and $Y_{dyn,src}$ and Y_{qs} placed in parallel.

thickness. The equivalent circuit is shown in Fig. 13, and all its components will be discussed in this section.

The admittance associated with the dynamic component of the current can be calculated with the following integral in the k_x complex plane extending to the dipoles the procedure presented for the slots in [27]:

$$Y_{dyn} = -\frac{1}{2\pi}\int_{-\infty}^{+\infty} \frac{2k_{xp}\,\mathrm{sinc}^2(k_x\Delta/2)}{D'(k_{xp})(k_x^2 - k_{xp}^2)}dk_x \tag{35}$$

whose solution is derived in Appendix D, and is written as follows:

$$Y_{dyn} = Y_{dyn,dip} + Y_{dyn,src} \tag{36}$$

where $Y_{dyn,dip}$ is associated with the propagation along the dipole and expressed as follows:

$$Y_{dyn,dip} = -\frac{j}{D'(k_{xp})}\,\mathrm{sinc}^2\left(\frac{k_{xp}\Delta}{2}\right) = \frac{1}{2Z_0}n^2 \tag{37}$$

and $Y_{dyn,src}$ is associated with the standing wave confined inside the source and calculated with the following analytical expression:

$$Y_{dyn,src} = \frac{2\left(\mathrm{sinc}(k_{xp}\Delta) - 1\right)}{\Delta k_{xp} D'(k_{xp})}. \tag{38}$$

Then, one can derive the transmission line equivalent circuit shown in Fig. 13, where two transmission line sections of characteristic impedance Z_0 are connected in series to a transformer of turn ratio n, and placed in parallel with $Y_{dyn,src}$. The dynamic admittance Y_{dyn} represents only the admittance associated with modal current waves traveling along the dipole with propagation constant k_{xp}, while the quasi-static effect of the gap has to be separately taken into account. This corresponds to the opportune modeling of the fast-varying current in the gap area, that were highlighted in the insets of Fig. 11.

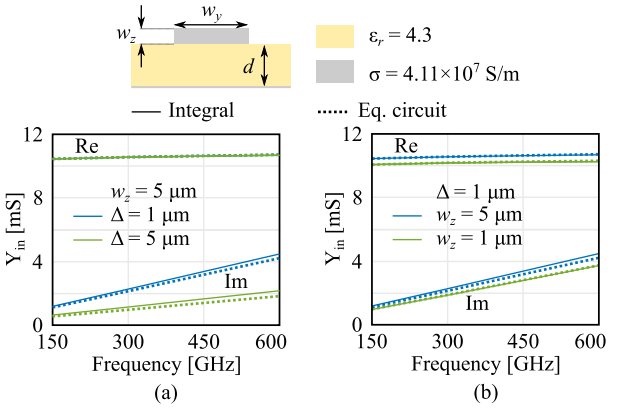

Fig. 14. Comparison of the input admittance calculated with the full spectral integral and with the equivalent circuit of a dipole constituted by a metal with conductivity $\sigma = 4.11 \times 10^7$ S/m and width $w_y = 20$ μm, and printed on a grounded dielectric slab with permittivity $\varepsilon_r = 4.3$, and thickness $d = 10$ μm for (a) fixed value of the metal thickness and different gap lengths and (b) fixed gap length and different metal thicknesses.

C. Quasi-Static Admittance

One can define the quasi-static admittance by using the following expression:

$$Y_{qs} = \frac{1}{2\pi}\int_{-\infty}^{+\infty} \frac{\mathrm{sinc}^2(k_x\Delta/2) - \mathrm{sinc}^2(k_x\Delta_{large}/2)}{D_\infty(k_x)}dk_x \tag{39}$$

where Δ_{large} is a feeding gap much larger than Δ, typically in the order of $\lambda_0/10$. The admittance Y_{qs} represents the reactance associated with the capacitive effect given by the fields fringing around the feeding gap. The numerator of (39) isolates the capacitance of the gap of size Δ. In fact, the subtraction operates as a filter that removes the low part of the spectrum, while the quasi-static component is left untouched as this component is negligible for Δ_{large}. As shown in Fig. 11, the impact of the quasi-static component of the current increases when decreasing the gap size or increasing the metal thickness, as these two parameters increase the gap capacitance. The definition of the quasi-static admittance Y_{qs} allows us to derive the transmission line equivalent circuit shown in Fig. 13, where Y_{qs} is placed in parallel with Y_{dyn}.

While the concept of dynamic admittance is meaningful only in the presence of a dominant polar contribution (e.g., in a mictrostrip), the quasi-static component can always be defined.

In Fig. 14, the input admittance of a dipole obtained by integrating (13) on the gap is compared with the one calculated with its transmission line equivalent circuit. The dipole is constituted by a metal having a conductivity $\sigma = 4.11 \times 10^7$ S/m and width $w_y = 20$ μm, and it is printed on a grounded dielectric slab having permittivity $\varepsilon_r = 4.3$ and thickness $d = 10$ μm. In Fig. 14(a), the input admittance is calculated for a metal thickness $w_z = 5$ μm and for the length of the feeding port $\Delta = 1$ μm and $\Delta = 5$ μm. For every value of Δ, there is an excellent agreement between the values obtained with the full integration and those obtained

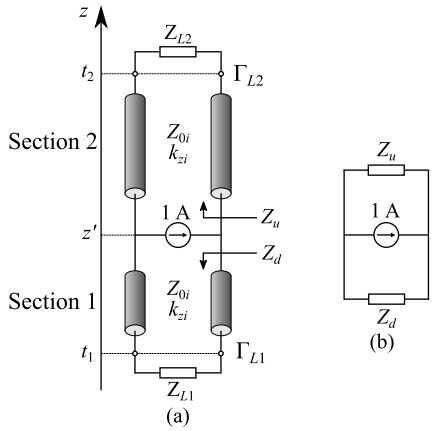

Fig. 15. (a) Transmission line circuit. (b) Lumped element circuit.

with the equivalent circuit. Moreover, one can recognize the effect of the shunt capacitance associated with the gap, as the imaginary part increases when decreasing Δ, leaving the real part unaffected. In Fig. 14(b) in turn, the input admittance is studied for $\Delta = 1\,\mu$m, for different values of the metal thickness. This latter affects both the real and imaginary parts, as it impacts both the characteristic impedance of the line and the capacitance of the feeding gap.

V. Conclusion

In this contribution, we derive a TL GF formalism to model dipoles with nonzero metal thickness. Thanks to the spectral domain formalism, the procedure can be used to efficiently analyze dipoles embedded in an arbitrary stratification, and allowing the analysis of microstrips and dipoles printed at the interface of two media radiating leaky waves. By comparison with state-of-the-art numerical techniques, up-to-par performances are shown. Finally, a transmission line equivalent circuit is derived, allowing for a deep physical insight on the propagation mechanism along the dipole, and on the effect of the feeding gap.

Appendix A
Derivation of the Formulation for the Potential of [18]

In the transmission line equivalent problem of Fig. 1(c), with the positive z-axis oriented upward and the unitary current source located at z', the voltage solution at $z \in [t_1;\ t_2]$ can be expressed as the sum of two terms. One models the propagation in an infinite transmission line with characteristic impedance Z_{0i} and propagation constant k_{zi}, while the other one accounts for the reflections given by the discontinuities at $z = t_1$ and $z = t_2$. This problem can be simplified with the transmission line sketched in Fig. 15(a), where the loads Z_{L1} and Z_{L2} are the impedances seen at $z = t_1$ and $z = t_2$, looking downward and upward, respectively. The voltage at z is given by the following expressions:

$$v_1(z) = V_1^+ e^{jk_{zi}z}\left(1 + \Gamma_{L1}e^{j2k_{zi}(t_1-z)}\right) \tag{40}$$

$$v_2(z) = V_2^+ e^{-jk_{zi}z}\left(1 + \Gamma_{L2}e^{-j2k_{zi}(t_2-z)}\right) \tag{41}$$

where 1 and 2 denote the section below and above the source, respectively, and

$$\Gamma_{L1} = \frac{Z_{L1} - Z_{0i}}{Z_{L1} + Z_{0i}} \tag{42}$$

$$\Gamma_{L2} = \frac{Z_{L2} - Z_{0i}}{Z_{L2} + Z_{0i}} \tag{43}$$

are the reflection coefficients between the loads Z_{LI} and Z_{L2} and the line, calculated at $z = t_1$ and $z = t_2$, respectively.

By enforcing the voltage at z' to be equal to the input impedance Z_{in} multiplied by the 1-A excitation, one can derive the following expressions for V_1^+ and V_2^+:

$$V_1^+ = Z_{\text{in}}\frac{e^{-jk_{zi}z'}}{1 + \Gamma_{L1}e^{j2k_{zi}(t_1-z')}} \tag{44}$$

$$V_2^+ = Z_{\text{in}}\frac{e^{jk_{zi}z'}}{1 + \Gamma_{L2}e^{-j2k_{zi}(t_2-z')}} \tag{45}$$

which yield to the following expressions for $v_1(z)$ $v_2(z)$:

$$v_1(z) = Z_{\text{in}}\frac{1 + \Gamma_{L1}e^{j2k_{zi}(t_1-z)}}{1 + \Gamma_{L1}e^{j2k_{zi}(t_1-z')}}e^{jk_{zi}(z-z')} \tag{46}$$

$$v_2(z) = Z_{\text{in}}\frac{1 + \Gamma_{L2}e^{-j2k_{zi}(t_2-z)}}{1 + \Gamma_{L2}e^{-j2k_{zi}(t_2-z')}}e^{-jk_{zi}(z-z')}. \tag{47}$$

The input impedance Z_{in} is the parallel between Z_u and Z_d, i.e., the impedances seen at z'_+ upward and z'_- downward, respectively. Z_d and Z_u can be expressed as follows:

$$Z_d = Z_{0i}\frac{1 + \Gamma_{L1}e^{j2k_{zi}(t_1-z')}}{1 - \Gamma_{L1}e^{j2k_{zi}(t_1-z')}} \tag{48}$$

$$Z_u = Z_{0i}\frac{1 + \Gamma_{L2}e^{-j2k_{zi}(t_2-z')}}{1 - \Gamma_{L2}e^{-j2k_{zi}(t_2-z')}} \tag{49}$$

which allow us to calculate Z_{in} as their parallel as follows:

$$Z_{\text{in}} = \frac{Z_{0i}}{2}\frac{\left(1 + \Gamma_{L2}e^{-j2k_{zi}(t_2-z')}\right)\left(1 + \Gamma_{L1}e^{j2k_{zi}(t_1-z')}\right)}{1 - \Gamma_{L1}\Gamma_{L2}e^{-j2k_{zi}(t_2-t_1)}}. \tag{50}$$

By using (50) in (46) and (47), one obtains the following expressions:

$$v_1(z) = \frac{Z_{0i}}{2}\frac{\left(1 + \Gamma_{L1}e^{j2k_{zi}(t_1-z)}\right)\left(1 + \Gamma_{L2}e^{-j2k_{zi}(t_2-z')}\right)}{1 - \Gamma_{L1}\Gamma_{L2}e^{-j2k_{zi}(t_2-t_1)}} \times e^{jk_{zi}(z-z')} \tag{51}$$

$$v_2(z) = \frac{Z_{0i}}{2}\frac{\left(1 + \Gamma_{L1}e^{j2k_{z}(t_1-z')}\right)\left(1 + \Gamma_{L2}e^{-j2k_{zi}(t_2-z)}\right)}{1 - \Gamma_{L1}\Gamma_{L2}e^{-j2k_{zi}(t_2-t_1)}} \times e^{-jk_{zi}(z-z')}. \tag{52}$$

By calculating the products in (51) and (52), one can write the following voltage expression:

$$v_1(z) = \frac{Z_{0i}}{2}\left(e^{jk_{zi}(z-z')} + Q(z,z')\right) \tag{53}$$

$$v_2(z) = \frac{Z_{0i}}{2}\left(e^{-jk_{zi}(z-z')} + Q(z,z')\right) \tag{54}$$

where

$$Q(z,z') = \frac{\Gamma_{L2}e^{-jk_{zi}(2t_2-z-z')} + \Gamma_{L1}e^{-jk_{zi}(z+z'-2t_1)}}{1 - \Gamma_{L1}\Gamma_{L2}e^{-j2k_{zi}(t_2-t_1)}}$$

$$+\frac{2\Gamma_{L1}\Gamma_{L2}e^{-j2k_{zi}(t_2-t_1)}\cos\left[k_{zi}(z-z')\right]}{1-\Gamma_{L1}\Gamma_{L2}e^{-j2k_{zi}(t_2-t_1)}}. \quad (55)$$

Therefore, one can write the following expression which is valid in either regions 1 and 2:

$$v(z)=\frac{Z_{0i}}{2}\left(e^{-jk_{zi}|z-z'|}+Q(z,z')\right) \quad (56)$$

Appendix B
Dynamic Current Space Distribution

Given the expression of the spectrum of the dynamic current (31), its space domain expression can be conveniently written as follows:

$$i_{\text{dyn}}(x)=f(x)*\frac{1}{\Delta}\text{rect}\left(\frac{x}{\Delta}\right)=\frac{1}{\Delta}\int_{-\Delta/2}^{\Delta/2}f(x-x')dx' \quad (57)$$

where f is a function to be determined, whose spectrum is defined in (31), and which can be calculated with the following inverse Fourier transform:

$$f(x)=\frac{1}{2\pi}\int_{-\infty}^{+\infty}\frac{2k_{xp}}{D'(k_{xp})(k_x-k_{xp})(k_x+k_{xp})}e^{-jk_xx}dk_x. \quad (58)$$

The considerations regarding the integral (58) are the same for (29). However, as we want do derive an analytical expression for f, both $x<0$ and $x>0$ must be considered. By combining the expressions resulting from the two conditions, one obtains $f(x)$ as follows:

$$f(x)=-j\frac{e^{-jk_{xp}|x|}}{D'(k_{xp})} \quad (59)$$

which is a single expression valid for every value of x.

Consequently, one can calculate the dynamic current as follows:

$$i_{\text{dyn}}(x)=-\frac{j}{\Delta D'(k_{xp})}\int_{-\Delta/2}^{\Delta/2}e^{-jk_{xp}|x-x'|}dx' \quad (60)$$

where, due to the absolute value at the exponent, different approaches have to be used.

If $x<-\Delta/2$ or $x>\Delta/2$, (60) is written as follows:

$$-\frac{je^{\mp jk_{xp}x}}{\Delta D'(k_{xp})}\int_{-\Delta/2}^{\Delta/2}e^{\pm jk_{xp}x'}dx' \quad (61)$$

where the choice of the signs at the exponent is for $x>\Delta/2$ and $x<-\Delta/2$, respectively, and by calculating the integral, one finds (32).

If $-\Delta/2<x<\Delta/2$, one can define the change of variable $x''=x-x'$, write (60) as follows:

$$-\frac{j}{\Delta D'(k_{xp})}\int_{x-\Delta/2}^{x+\Delta/2}e^{-jk_{xp}|x''|}dx'' \quad (62)$$

and expand the absolute value as follows:

$$-\frac{j}{\Delta D'(k_{xp})}\left(\int_{x-\Delta/2}^{0}e^{jk_{xp}x''}dx''+\int_{0}^{x+\Delta/2}e^{-jk_{xp}x''}dx''\right) \quad (63)$$

and finally, by integration, one obtains (33).

Appendix C
Asymptotic

By recalling the definition of the sinc function

$$\text{sinc}\left(\frac{k_yw_y}{2}\right)=\frac{1}{w_y}\int_{-w_y/2}^{w_y/2}e^{jk_yy}dy \quad (64)$$

the integral between $-w_y/2$ and $w_y/2$ can be written as the superposition of three contributions as follows:

$$\frac{1}{w_y}\left(\int_{-\infty}^{+\infty}e^{jk_yy}dy-\int_{-\infty}^{-w_y/2}e^{jk_yy}dy-\int_{w_y/2}^{+\infty}e^{jk_yy}dy\right). \quad (65)$$

By substituting (65) into (14), one obtains the following expression:

$$D(k_x)=D_0+D_1(k_x)+D_2(k_x) \quad (66)$$

where

$$D_0=\rho\langle j_t,\tilde{j}_t\rangle_A \quad (67)$$

$$D_1(k_x)=-\frac{J_{t,y}(0)}{w_y}\int_0^{w_z}\int_0^{w_z}\left[G_{xx}^{EJ}(k_x,0,z,z')\times j_{t,z}(z')\tilde{j}_{t,z}^*(z)\right]dzdz' \quad (68)$$

$$D_2(k_x)=\frac{1}{2\pi w_y}\int_{C_\infty}\left[\int_0^{w_z}\int_0^{w_z}\left(\int_{-\infty}^{+\infty}G_{xx}^{EJ}(k_x,k_y,z,z')\times J_{t,y}(k_y)e^{jk_yy}dk_y\right)j_{t,z}(z')\tilde{j}_{t,z}^*(z)dzdz'\right]dy \quad (69)$$

with $C_\infty=[-\infty,-w_y/2]\cup[w_y/2,+\infty]$. For large values of k_x, k_z has a large imaginary part, making the propagation along z strongly attenuated. Therefore the contributions of the reflections are negligible, and the source can be represented as to be radiating in a homogeneous medium, as shown in Fig. 16. The integral between the round brackets in (69) can be written in the following form:

$$(k^2-k_x^2)\int_{-\infty}^{+\infty}\frac{J_0(k_yw_y/2)}{\sqrt{k^2-k_x^2-k_y^2}}e^{jk_yy'}dk_y \quad (70)$$

where J_0 is the first-kind zeroth-order Bessel function and the homogeneous space Green's function has been used. The solution of (70) can be seen as the field radiated at $y'\in C_\infty$ by lines of current located between $-w_y/2$ and $w_y/2$ and having the profile of j_{ty} and having expression

$$\pi(k^2-k_x^2)H_0^{(2)}\left(\sqrt{k^2-k_x^2}|y'|\right)*j_{ty}(y') \quad (71)$$

where $H_0^{(2)}$ is the second kind zeroth order Hankel function. For $k_x\to\infty$, the Hankel function represents a spatial decay, which can be made arbitrarily small. Therefore, the contribution of (69) results negligible with respect to (67) and (68).

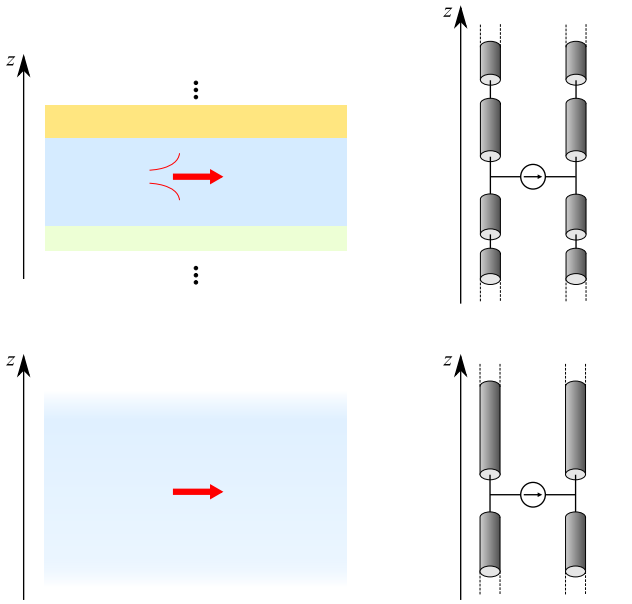

Fig. 16. Sketch of cut-off modes propagating in stratified media and their equivalent propagation in a homogeneous medium.

Appendix D
Dynamic Admittance

The dynamic admittance Y_{dyn} is defined with the spectral domain integral (35) and due to its integrand function can be expressed—in a similar fashion as (57)—with the following space integrals:

$$Y_{\text{dyn}} = \frac{1}{\Delta^2}\int_{-\Delta/2}^{\Delta/2}\int_{-\Delta/2}^{\Delta/2} f\left(x-x'\right)dx\,dx' \tag{72}$$

where the function f is the same as (59), and which allows us to express Y_{dyn} as follows:

$$Y_{\text{dyn}} = -\frac{j}{D'\left(k_{xp}\right)\Delta^2}\int_{-\Delta/2}^{\Delta/2}\left(\int_{-\Delta/2}^{\Delta/2} e^{-jk_{xp}|x-x'|}dx'\right)dx. \tag{73}$$

The integral in brackets can be calculated as in (63), which results into (33), allowing us to calculate the dynamic admittance with the following single integral:

$$-\frac{2}{D'\left(k_{xp}\right)\Delta k_{xp}}\int_{-\Delta/2}^{\Delta/2}\left(1-\cos\left(k_{xp}x\right)e^{-jk_{xp}\Delta/2}\right)dx \tag{74}$$

which can be closed into the following expression:

$$\frac{2}{D'\left(k_{xp}\right)\Delta k_{xp}}\left(e^{-jk_{xp}\Delta/2}\,\text{sinc}\left(k_{xp}\Delta/2\right)-1\right). \tag{75}$$

By expanding the complex exponential in (75) into sine and cosine and by using the identity $\cos(x)\,\text{sinc}(x) = \text{sinc}(2x)$, (75) can be rewritten as follows:

$$\frac{2\left(\text{sinc}\left(k_{xp}\Delta\right)-1\right)}{\Delta k_{xp}D'\left(k_{xp}\right)} - \frac{j}{D'\left(k_{xp}\right)}\,\text{sinc}^2\left(\frac{k_{xp}\Delta}{2}\right) \tag{76}$$

which yields (36)–(38).

References

[1] R. Garg, I. Bahl, and M. Bozzi, *Microstrip Lines and Slotlines*, 3rd ed. Norwood, MA, USA: Artech House, 2013.

[2] *Sonnet*, Sonnet Softw., Syracuse, NY, USA, 2023.

[3] *CST Studio Suite*, Dassault Systèmes, Vélizy-Villacoublay, France, 2023.

[4] *Ansys Electronics*, Ansys, Canonsburg, PA, USA, 2023.

[5] *Advanced Design System*, Keysight, Santa Rosa, CA, USA, 2023.

[6] C. Di Nallo, F. Mesa, and D. R. Jackson, "Excitation of leaky modes on multilayer stripline structures," *IEEE Trans. Microw. Theory Techn.*, vol. 46, no. 8, pp. 1062–1071, Aug. 1998.

[7] P. Burghignoli, C. Di Nallo, F. Frezza, A. Galli, and P. Lampariello, "Efficient description of impedance and radiation features in printed-circuit leaky-wave structures—An unconventional scattering-matrix approach," *IEEE Trans. Microw. Theory Techn.*, vol. 48, no. 10, pp. 1661–1672, Oct. 2000.

[8] A. Neto and S. Maci, "Green's function for an infinite slot printed between two homogeneous dielectrics. I. Magnetic currents," *IEEE Trans. Antennas Propag.*, vol. 51, no. 7, pp. 1572–1581, Jul. 2003.

[9] J. Bernal, F. Mesa, and D. R. Jackson, "Effects of losses on the current spectrum of a printed-circuit line," *IEEE Trans. Microw. Theory Techn.*, vol. 55, no. 7, pp. 1511–1519, Jul. 2007.

[10] J. Bernal, F. Mesa, D. R. Jackson, W. L. Langston, and J. T. Williams, "High-frequency pulse distortion on a lossy microstrip line with a top cover," *IEEE Trans. Microw. Theory Techn.*, vol. 58, no. 7, pp. 1774–1785, Jul. 2010.

[11] S. Paulotto, G. Lovat, P. Baccarelli, and P. Burghignoli, "Green's function calculation for a line source exciting a 2-D periodic printed structure," *IEEE Microw. Wireless Compon. Lett.*, vol. 20, no. 4, pp. 181–183, Apr. 2010.

[12] S. Bruni, "The ultrawideband leaky lens antenna," *IEEE Trans. Antennas Propag.*, vol. 55, no. 10, pp. 2642–2653, Oct. 2007.

[13] R. M. van Schelven, D. Cavallo, and A. Neto, "Equivalent circuit models of finite slot antennas," *IEEE Trans. Antennas Propag.*, vol. 67, no. 7, pp. 4367–4376, Jul. 2019.

[14] A. Neto and J. J. Lee, "'Infinite bandwidth' long slot array antenna," *IEEE Antennas Wireless Propag. Lett.*, vol. 4, pp. 75–78, 2005.

[15] TS Group. *Transmission Line Calculator*. Accessed: Oct. 1, 2023. [Online]. Available: https://terahertz.tudelft.nl/Research/project.php?id=74&ti=27

[16] S. L. van Berkel, A. Garufo, N. Llombart, and A. Neto, "A quasi-analytical tool for the characterization of transmission lines at high frequencies [EM programmer's notebook]," *IEEE Antennas Propag. Mag.*, vol. 58, no. 3, pp. 82–90, Jun. 2016.

[17] D. Cavallo, "Connected array antennas: Analysis and design," Ph.D. dissertation, Dept. Elect. Eng., Eindhoven Univ. Technol., Eindhoven, The Netherlands, 2011.

[18] K. A. Michalski and D. Zheng, "Electromagnetic scattering and radiation by surfaces of arbitrary shape in layered media. I. Theory," *IEEE Trans. Antennas Propag.*, vol. 38, no. 3, pp. 335–344, Mar. 1990.

[19] S. Ramo, J. R. Whinnery, and T. van Duzer, *Fields and Waves in Communication Electronics*. Hoboken, NJ, USA: Wiley, 1994, ch. 3, sec. 16, pp. 149–153.

[20] D. S. Jones, *Methods in Electromagnetic Wave Propagation*. Piscataway, NJ, USA: IEEE Press, 1995.

[21] D. Cavallo, W. H. Syed, and A. Neto, "Equivalent transmission line models for the analysis of edge effects in finite connected and tightly coupled arrays," *IEEE Trans. Antennas Propag.*, vol. 65, no. 4, pp. 1788–1796, Apr. 2017.

[22] N. K. Das, "A new theory of the characteristic impedance of general printed transmission lines applicable when power leakage exists," *IEEE Trans. Microw. Theory Techn.*, vol. 48, no. 7, pp. 1108–1117, Jul. 2000.

[23] F. Mesa and D. R. Jackson, "A novel approach for calculating the characteristic impedance of printed-circuit lines," *IEEE Microw. Wireless Compon. Lett.*, vol. 15, no. 4, pp. 283–285, Apr. 2005.

[24] J. C. Rautio and V. Demir, "Microstrip conductor loss models for electromagnetic analysis," *IEEE Trans. Microw. Theory Techn.*, vol. 51, no. 3, pp. 915–921, Mar. 2003.

[25] E. M. Hamham, F. Mesa, F. Medina, and M. Khalladi, "Surface-impedance quasi-transverse electromagnetic approach for the efficient calculation of conductor losses in multilayer single and coupled microstrip lines," *IET Microw., Antennas Propag.*, vol. 6, no. 5, pp. 519–526, 2012.

[26] J. Aguilera, R. Marques, and M. Horno, "Quasi-TEM surface impedance approaches for the analysis of MIC and MMIC transmission lines, including both conductor and substrate losses," *IEEE Trans. Microw. Theory Techn.*, vol. 43, no. 7, pp. 1553–1558, Jul. 1995.

[27] A. Neto and S. Maci, "Input impedance of slots printed between two dielectric media and fed by a small Δ-gap," *IEEE Antennas Wireless Propag. Lett.*, vol. 3, pp. 113–116, 2004.

[28] D. Cavallo, A. Neto, and G. Gerini, "Green's function based equivalent circuits for connected arrays in transmission and in reception," *IEEE Trans. Antennas Propag.*, vol. 59, no. 5, pp. 1535–1545, May 2011.

[29] R. Rodriguez-Berral, F. Mesa, and D. R. Jackson, "A high-frequency circuit model for the gap excitation of a microstrip line," *IEEE Trans. Microw. Theory Techn.*, vol. 54, no. 12, pp. 4100–4110, Dec. 2006.

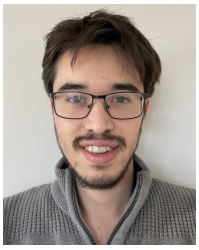

Erik A. Speksnijder received the B.Sc. and M.Sc. degrees (cum laude) in electrical engineering from the Delft University of Technology (TU Delft), Delft, The Netherlands, in 2021 and 2023, respectively.

He is currently an Antenna Scientist with the Netherlands Organization for Applied Scientific Research (TNO), The Hague, The Netherlands.

Riccardo Ozzola (Graduate Student Member, IEEE) received the B.Sc. and M.Sc. degrees (Hons.) from the University of Florence, Florence, Italy, in 2017 and 2019, respectively. He is currently pursuing the Ph.D. degree at the Delft University of Technology (TU Delft), Delft, The Netherlands.

His master thesis project was developed at the Terahertz Sensing Group, TU Delft. His current research interests include the theory and design of multibeam wideband arrays for wireless communications, the electromagnetic characterization of multiple-input and multiple-output (MIMO) systems, and the development of numerical methods for electromagnetics.

Mr. Ozzola was one of the Finalists for the Best Electromagnetics Paper Award at the European Conference on Antennas and Propagation (EuCAP) in 2021.

Andrea Neto (Fellow, IEEE) received the Laurea degree (summa cum laude) in electronic engineering from the University of Florence, Florence, Italy, in 1994, and the Ph.D. degree in electromagnetics from the University of Siena, Siena, Italy, in 2000.

Part of his Ph.D. degree was developed at the European Space Agency Research and Technology Center Noordwijk, Noordwijk, The Netherlands. He worked at the Antenna Section, European Space Agency Research and Technology Center, Noordwijk, for over two years. From 2000 to 2001, he was a Post-Doctoral Researcher with the California Institute of Technology, Pasadena, CA, USA, where he worked with the Submillimeter Wave Advanced Technology Group. From 2002 to January 2010, he was a Senior Antenna Scientist with TNO Defense, Security, and Safety, The Hague, The Netherlands. In February 2010, he became a Full Professor of applied electromagnetism with the EEMCS Department, Technical University of Delft, Delft, The Netherlands, where he formed and leads the THz Sensing Group. He published over 300 journals and conference papers in the field of applied electromagnetism. His research interests include the analysis and design of antennas with an emphasis on arrays, dielectric lens antennas, wideband antennas, electromagnetic band-gap (EBG) structures, and terahertz (THz) antennas.

Dr. Neto is a Technical Board Member of the European School of Antennas and an Organizer of the course on antenna imaging techniques. He was a recipient of the H. A. Wheeler Award for the best applications paper of IEEE TRANSACTIONS ON ANTENNAS AND PROPAGATION in 2008 and the European Research Council Starting Grant to perform research on advanced antenna architectures for THz sensing systems, in 2011. He served as an Associate Editor for IEEE TRANSACTIONS ON ANTENNAS AND PROPAGATION from 2008 to 2013 and IEEE ANTENNAS AND WIRELESS PROPAGATION LETTERS from 2005 to 2013, and IEEE TRANSACTIONS ON TERAHERTZ SCIENCE AND TECHNOLOGY since 2023.